PAPER

Check for updates

Enhanced formaldehyde gas-sensing response based on indium oxide nanowires doped with same-valence metal cations

J. Y. Niu, B. Hong, J. C. Xu, [ID] Y. B. Han, H. X. Jin, D. F. Jin, Y. X. Zeng, X. L. Peng, H. L. Ge and X. Q. Wang [ID] *

Mesoporous indium oxides nanowires (In_2O_3 NWs) doped with Al, Sb and La were synthesized using a nanocasting method, and then the components, microstructures and morphology were characterized. All results indicate that the doped metals are well dispersed in the In_2O_3 NWs and hardly affect the NW microstructure and morphology. While the cations-doped concentration decreases greatly with the increasing radii of Al, Sb and La cations. The cation-doping not only causes the lattice distortion to improve the adsorbed oxygen on the surface, but also increases the ground-state resistance of the In_2O_3 NWs. In this way, the cation-doping greatly affects the gas-sensing behavior of formaldehyde gas. Considering the resistance in air and formaldehyde gas, the $In_{1.984}La_{0.016}O_3$ NW sensor exhibits the best gas-sensing performance of 10 ppm formaldehyde gas with a response of 39.51 at 210 °C owing to the largest radius and lowest doping content of La^{3+}.

1. Introduction

Formaldehyde (HCHO) is the simplest aldehyde, and is a colorless irritating gas.[1] Long-term exposure to HCHO gas at a concentration higher than 0.1 ppm may cause serious eye irritation, a burning sensation in the throat, dyspnea, asthma-related symptoms and cancer.[2] Considering the health hazards to humans and animals, it is very important to monitor the concentration of HCHO gas both indoors and outdoors.[3] Therefore, test instruments and techniques should be well developed to detect and monitor HCHO gas in real-time.[4] Nowadays, gas chromatography,[5] high performance liquid chromatography,[6] colorimetry-based derivatization,[7] protein-based biosensing systems[8] and gas sensors[9,10] have been developed and used in formaldehyde monitoring.

Gas sensors based on metal oxide semiconductors (MOS) have been well studied and developed to detect and monitor poisonous and harmful gases.[11] The gas response of a MOS sensor is defined as the ratio of the resistance in target gas to that in air.[12] For gas sensors it is important to control the microstructure of the material, to increase the specific surface area of MOS nanostructure. Nowadays, one-dimensional MOS nanostructures are widely studied as gas-sensing mediums due to their very large surface-to-volume ratio, high specific surface area and high porosity.[13–15] In recent years, nanowires (NWs) have been used widely in gas sensors. For example, Wang *et al.*

synthesized mesoporous Co_3O_4 NWs using a nanocasting method, and these NWs indicated an excellent gas-sensing performance for toluene gas.[16] Hassen *et al.* fabricated rGO-$W_{18}O_{49}$ NWs, improving the gas-sensing response to toluene gas.[17] However, microstructural regulation only improves the surface area to some extent.

As is known, heterogeneous doping can effectively adjust the carrier concentration of one-dimensional MOS nanostructures.[18] Heterogeneous doping not only adjusts the resistance in the ground state but also causes lattice distortion of the MOS nanostructure. This lattice distortion results in more oxygen vacancies, which leads to more adsorbed oxygen on MOS nano-structures. Chen *et al.* synthesized high-valence-cation-doped NiO NWs, and the responses of the NiO NW sensor was greatly increased with doping of the high-valence donors.[19] Mokoena *et al.* studied a Eu^{3+}-doped NiO sensor for toluene gas detection, and the response was higher than for the NiO sensor.[21]

Due to its broad bandgap, low cost, low resistivity and high catalytic activity, In_2O_3 nanostructures as n-type MOS have been widely investigated all over the world to improve the gas-sensing performance.[22] Jin *et al.* synthesized hierarchical porous In_2O_3 nanospheres, the sensor for which showed better selectivity for TEA and ethanol.[23] Liu *et al.* prepared Sb-doped In_2O_3 microstructures for acetone detection, which showed a higher response compares with In_2O_3.[24] Liang *et al.* synthesized Ca-doped In_2O_3 nanotubes, which showed excellent selectivity and a high response toward formaldehyde.[25]

In order to more accurately reveal the influence of lattice distortion from cation-doping, the interference of the carrier

College of Materials Science and Chemistry, China Jiliang University, Hangzhou, 310018, China. E-mail: wxqnano@cjlu.edu.cn

concentration, morphology, average particle size and specific surface area on the gas-sensing behavior of In_2O_3 nanostructures should be excluded.[26] In this paper, a nanocasting method and the same process conditions were used to synthesize In_2O_3 NWs and cation-doped In_2O_3 NWs with a similar diameter, microstructure and specific surface area. The cations Al^{3+}, Sb^{3+} and La^{3+} were doped into the In_2O_3 NWs using SBA-15 silica as a hard template. The influence of the doping content and cation radius on the microstructure and gas-sensing properties toward HCHO was investigated in detail. After optimizing the operating conditions of the In_2O_3 NW gas sensors, the physical mechanism was analyzed theoretically based on the doped semiconductor theory.

2. Experimental

2.1 Synthesis of In_2O_3 and cation-doped In_2O_3 NWs

All chemicals and reagents in this study were of analytical grade and used directly without further purification. The In_2O_3 NWs and Al-, Sb- and La-doped In_2O_3 NWs were synthesized using mesoporous SBA-15 silica as a hard template.19 Indium nitrates, aluminum chloride, antimony chloride, lanthanum nitrate and the SBA-15 powder were uniformly dissolved and dispersed in ethanol solution according to the atomic ratio of Si, *i.e.*, (In + Al, Sb and La):(Al, Sb and La) = 2:1:0.05, and then *n*-hexane was added. After evaporating the above solution, the obtained powder samples were calcined at 260 °C using a muffle furnace. After washing to remove undecomposed soluble salts, the powder samples were sintered in air at 600 °C for 6 h and the SBA-15 silica was removed using a 2 M NaOH aqueous solution. Compared with the In_2O_3 molecular formula, the cation-doped In_2O_3 NWs were denoted as $In_{2-x}M_xO_3$ (M = Al, Sb or La), in which x is the doping content calculated *via* EDS.

2.2 Characterization of microstructures and gas-sensing properties

The phases, morphology and microstructures of undoped and cation-doped In_2O_3 NWs were characterized *via* XRD (SmartLabSE, 3 kW, Cu target, wavelength 0.154 nm, step 0.02°),

TEM (JEOL, JEM-1400Flash, 120 kV), and EDS (HITACH, SU8010). Moreover, the bandgap and specific surface area were measured and deduced the from UV-visible adsorption spectra (UV3600 Spectrophotometer) and N_2 adsorption–desorption isotherms (ASAP2020 Surface Area and Porosity Analyzer, −196 °C, relative pressure of 0.06 to 0.2), respectively.

The gas-sensing tests were performed *via* static distribution using a CGS-4TPs gas-sensing measurement system with atmospheric air as the interference gas, where the relative humidity was held at about 30%. First, 2 mg In_2O_3 NWs or cation-doped In_2O_3 NWs and 1 ml deionized water were mixed together to form a homogeneous paste, which was brush-coated onto an Al_2O_3 ceramic substrate with interdigitated Ag–Pd electrodes. The as-prepared simulated sensors were dried in air at room temperature and then aged at 350 °C for 2 h in air to improve their stability. Considering the volume of the test chamber, the volume of HCHO liquid (37–40%), ammonia water (25–28%), water, ethanol, xylene, toluene and methanol were calculated, and then the above liquid was injected into the chamber and evaporated to a gas with a concentration from 1 ppm to 15 ppm. The response for n-type In_2O_3 NW sensors is defined as the ratio of the resistance in air (R_{air}) to that in HCHO gas (R_{gas}).[13]

3. Results and discussion

3.1 Microstructures and morphology of cation-doped In_2O_3 NWs

The phase analysis of In_2O_3 and cation-doped In_2O_3 NWs was performed using XRD, as shown in Fig. 1, in which all peaks are normalized according to the strongest (222) peak. The diffraction peaks of all the samples are consistent with the characteristic peaks of cubic In_2O_3 (PDF#71-2194). The diffraction peaks at 2θ values of 21.65, 30.76, 35.618, 51.188 and 60.85° correspond to the (211), (222), (400), (440) and (622) facets according to the standard card. The characteristic peaks belonging to Al-, Sb- and La-based compounds are not observed. The average crystallite sizes calculated using the Scherrer equation are listed in Table 1. In order to reveal the influence of doping with different cations
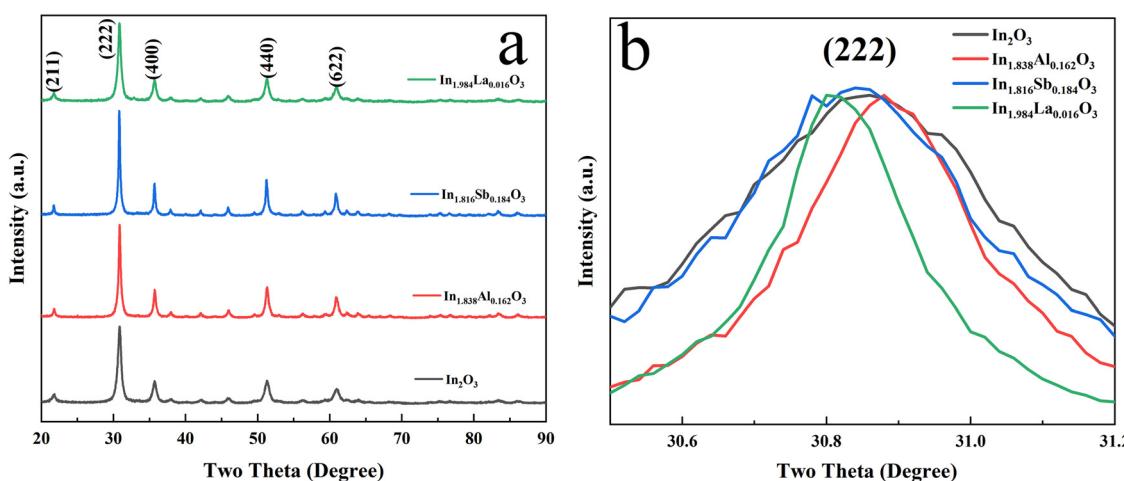

Fig. 1 Full-angle range of XRD patterns (a) and shift of the (222) peak (b) for undoped In_2O_3 and cation-doped In_2O_3 NWs.

Table 1 Structural and gas-sensing parameters of In_2O_3 and cation-doped In_2O_3 NWs

| Sample	Crystallite size (nm)	Average pore size (nm)	S_{BET} (m^2 g^{-1})	E_g (eV)	Response, S
In_2O_3	17.9	6.29520	57.37	3.34	26.16
$In_{1.838}Al_{0.162}O_3$	38.8	8.29376	53.55	3.39	28.73
$In_{1.816}Sb_{0.184}O_3$	45.8	7.82711	49.21	3.40	19.78
$In_{1.984}La_{0.016}O_3$	23.0	6.37254	57.29	3.36	39.51

on the lattice distortion of the In_2O_3 NWs, the (222) peaks of all the samples are enlarged and shown in Fig. 1b. Clearly, the (222) peak of the Al-doped In_2O_3 NWs is shifted to a higher angle and the La-doped sample shifted to a lower angle, while the Sb-doped In_2O_3 NWs are the same the In_2O_3 NWs due to the similar radius. According to Bragg's law:

$$2d\sin\theta = \lambda \tag{1}$$

where d is the distance between parallel atomic planes, λ is the incident wavelength and θ is the angle between the incident light and the crystal plane. In this way, La-doped In_2O_3 NWs should present a higher d for the larger radius of La^{3+} while Al-doped In_2O_3 NWs should possess a lower d for the lower Al^{3+} radius compared with In^{3+} according to eqn (1). Therefore, it is concluded that Al, Sb and La were successfully doped into the In_2O_3 lattice, which leads to the lattice distortion of the In_2O_3 NWs.[27]

The components of In_2O_3 and cation-doped In_2O_3 NWs are characterized *via* EDS in Fig. 2. Considering the atomic percentage of all samples, cation-doped In_2O_3 NWs can be expressed as $In_{1.838}Al_{0.162}O_3$, $In_{1.816}Sb_{0.184}O_3$ and $In_{1.984}La_{0.016}O_3$ NWs, respectively. Owing to the different cation radius values of In, Al, Sb and La in the initial solution, the probability of these cations entering the mesochannels of SBA-15 is different.[19] The probability of entering the mesochannels decreases greatly with the increasing radius of the doped cation. As a result, the $In_{1.838}Al_{0.162}O_3$ and $In_{1.816}Sb_{0.184}O_3$ NWs present the highest doping concentration while the $In_{1.984}La_{0.016}O_3$ NWs show the lowest doping concentration. Moreover, Fig. 3 shows the EDS spectra of $In_{1.838}Al_{0.162}O_3$, $In_{1.816}Sb_{0.184}O_3$ and $In_{1.984}La_{0.016}O_3$ NWs, indicating that Al, Sb and La are well-dispersed in the $In_{1.838}Al_{0.162}O_3$, $In_{1.826}Sb_{0.184}O_3$ and $In_{1.984}La_{0.016}O_3$ NWs. It can be seen easily from the number of bright spots that the La content is the lowest while the separate Al and Sb contents are much higher.

The morphology and microstructure of In_2O_3 and the cation-doped In_2O_3 NWs are observed using TEM in Fig. 4. It is shown that all samples exhibit mesoporous structures and that cation doping hardly affects the microstructure of the In_2O_3 NWs. The diameter of the nanowires is measured to be 8–9 nm and mesochannel size is about 2–3 nm.[28] The N_2 adsorption–desorption isotherms of In_2O_3 and the cation-doped In_2O_3 NWs are shown in Fig. 5. The curves of all samples exhibit type-IV adsorption isotherms, which are characteristic of mesoporous structures according to IUPAC. The BET surface area (S_{BET}) and average pore size of all the samples calculated from
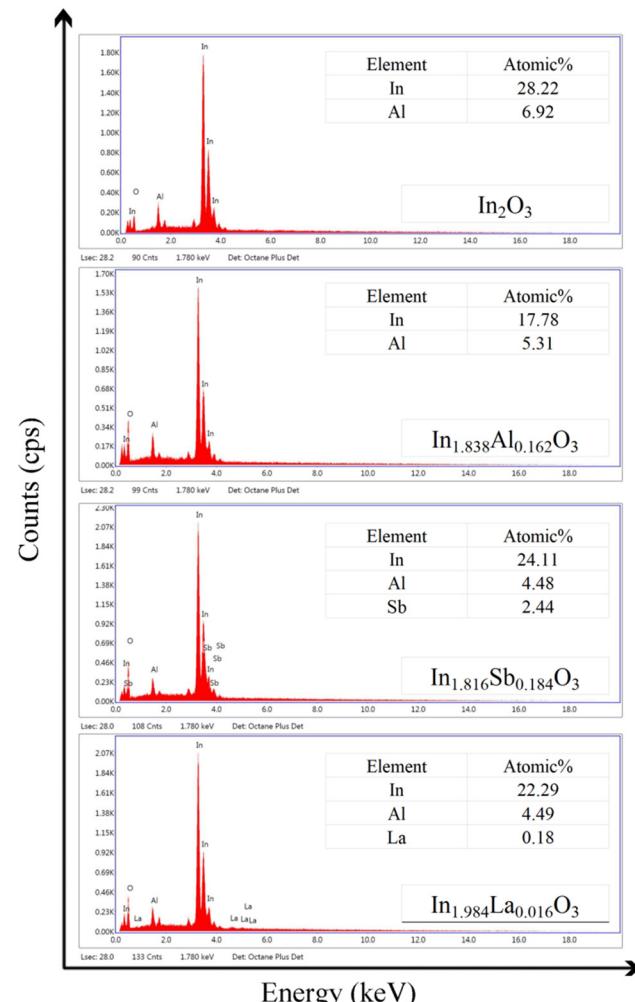
Fig. 2 EDS images of In_2O_3 and cation-doped In_2O_3 NWs.
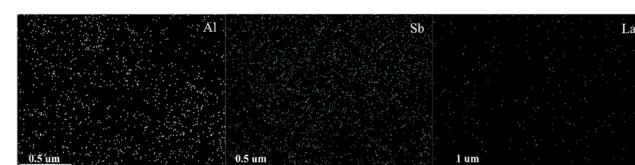
Fig. 3 Al, Sb and La EDS spectra of cation-doped In_2O_3 NWs.

the N_2 adsorption–desorption isotherm data are given in Table 1. The specific surface area changes a little from 49.2 m^2 g^{-1} to 57.4 m^2 g^{-1}. The pore size distribution diagrams of all the samples are shown in the insets of Fig. 5, in which the average pore size is mainly focused around 4–5 nm.

The UV-visible absorption spectra of In_2O_3 and the cation-doped In_2O_3 NWs are used to calculate the bandgap (E_g) in Fig. 6. E_g is the basis of the optical absorption spectra according to eqn (2):[29]

$$(\alpha h\nu)^{1/n} = A(h\nu - E_g) \tag{2}$$

where α is the absorption coefficient, h is the Planck constant, ν is the photon frequency, A is constant and n is the electronic
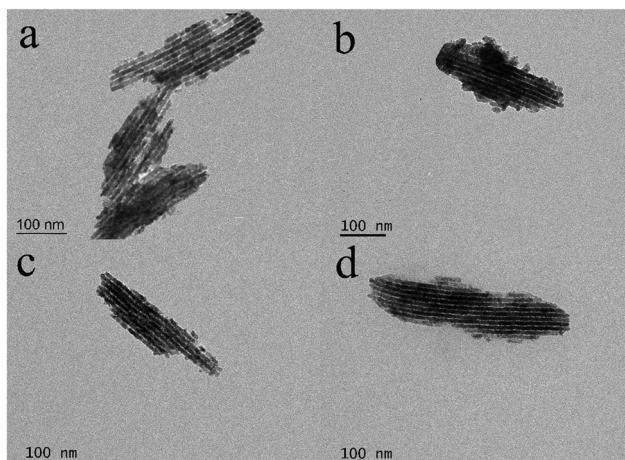
Fig. 4 TEM images of (a) In_2O_3, and (b) Al-, (c) Sb- and (d) La-doped In_2O_3 NWs.

transition parameter (which is equal to 1/2 for a direct bandgap semiconductor). Since α is proportional to the absorbance (A)

according to the Beer–Lambert law, the energy intercept of the curve of $(\alpha h\nu)^2$ *versus* $h\nu$ gives E_g when the linear region is extrapolated to the zero ordinate.[20] The E_g values of all the samples are given in Table 1, which shows that there is a small increase from 3.34 eV for the In_2O_3 NWs to about 3.40 eV for the cation-doped In_2O_3 NWs owing to lattice distortion.

3.2 Gas-sensing performance of cation-doped In_2O_3 NWs sensors

The gas-sensing behavior for 10 ppm HCHO gas of the In_2O_3 and cation-doped In_2O_3 NW sensors is characterized at operating temperatures from 190 to 240 °C in Fig. 7(a). For all the sensors, the response ($S = R_{air}/R_{gas}$) to HCHO gas increases initially up to a maximum value at 210 °C with increasing temperature, and then decreases to some extent. This phenomenon could be attributed to the balance of the surface chemical reaction and the HCHO gas diffusion. In this way, the operating temperature was confirmed to be 210 °C for all sensors in the subsequent experiments. Comparing all sensors, the response of the $In_{1.984}La_{0.016}O_3$ and
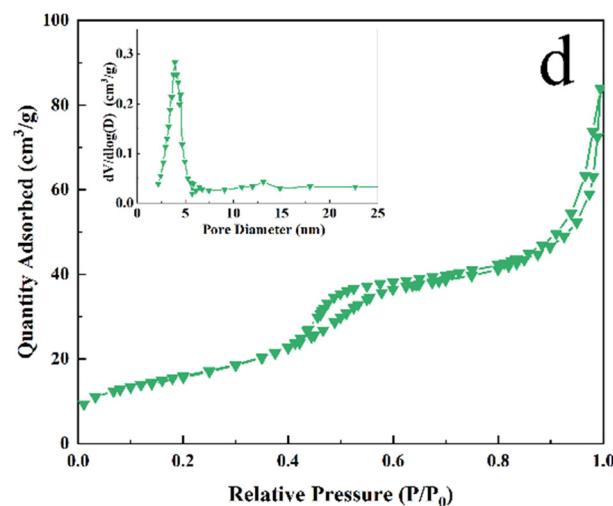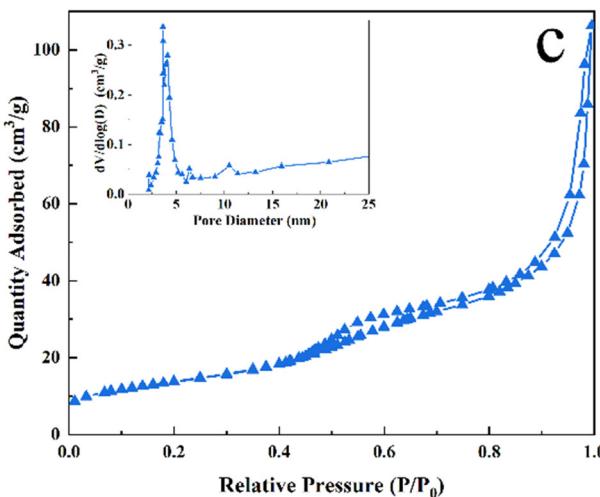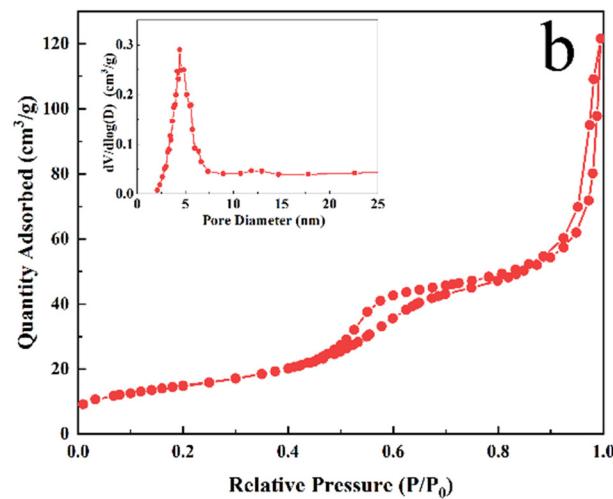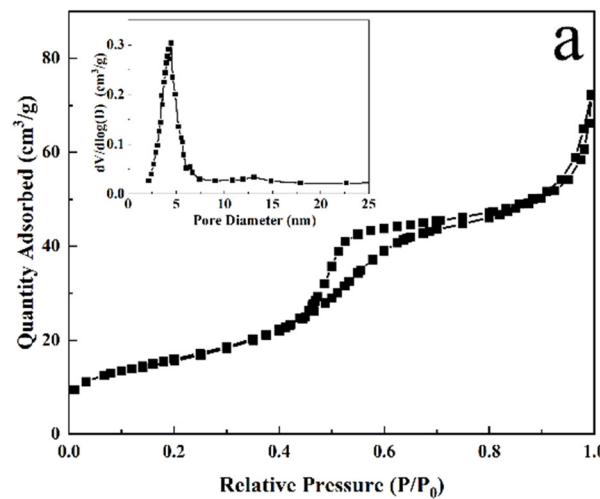

Fig. 5 N_2 adsorption–desorption isotherms and pore size distribution plots (inset) of (a) In_2O_3, and (b) Al-, (c) Sb- and (d) La-doped In_2O_3 NWs.
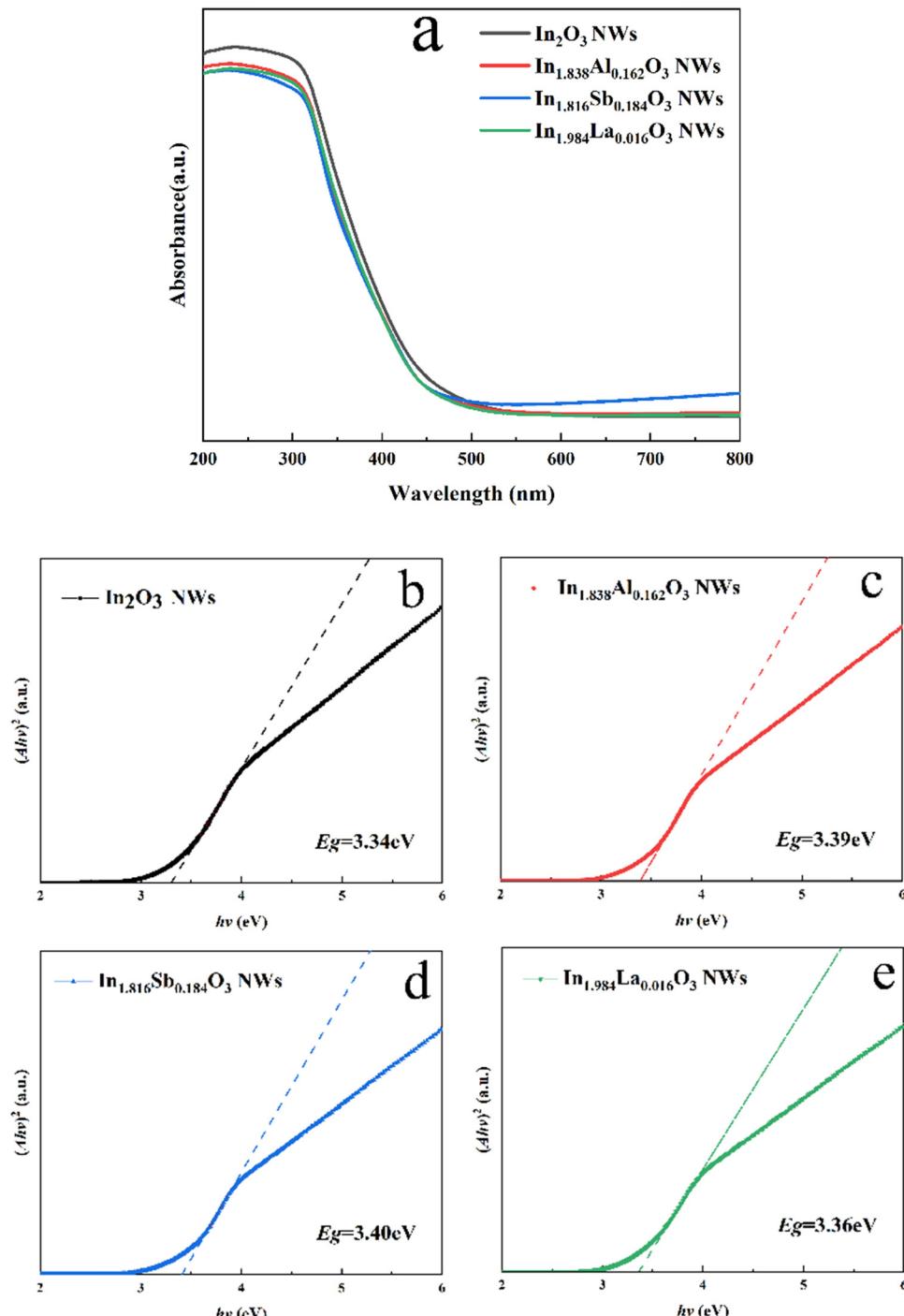
Fig. 6 UV-vis spectrum of (a) In_2O_3 and the cation-doped In_2O_3 NWs; and (b–e) plots of $(Ah\nu)^2$ *versus* $h\nu$ for (b) In_2O_3, and the (c) Al-, (d) Sb- and (e) La-doped In_2O_3 NWs.

$In_{1.838}Al_{0.162}O_3$ NWs sensors is higher than that of the In_2O_3 NW sensor, while the $In_{1.186}Sb_{0.184}O_3$ NWs sensor shows the lowest response to HCHO gas at 210 °C. The change in resistance for In_2O_3 and the cation-doped In_2O_3 NW sensors to 10 ppm HCHO gas at 210 °C is given in Fig. 7(b), for which the resistance values in air and HCHO gas are also listed in Table 2. Owing to the electron-depletion layer at the shell of In_2O_3 NWs in air from adsorbed oxygen, R_{air} for all the sensors is much larger than R_{gas}.

Furthermore, the differences in the resistance are relatively large due to the thickness differences of all the sensors. The R_{air} values of all the sensors at the different operating temperatures are given in Fig. 7(c), in which R_{air} decreases with the increasing temperature. The response and recovery time are defined as the time required for a change in the resistance to reach 90% of the equilibrium value after HCHO is injected and then removed. The response time for In_2O_3 and the cation-doped In_2O_3 NWs
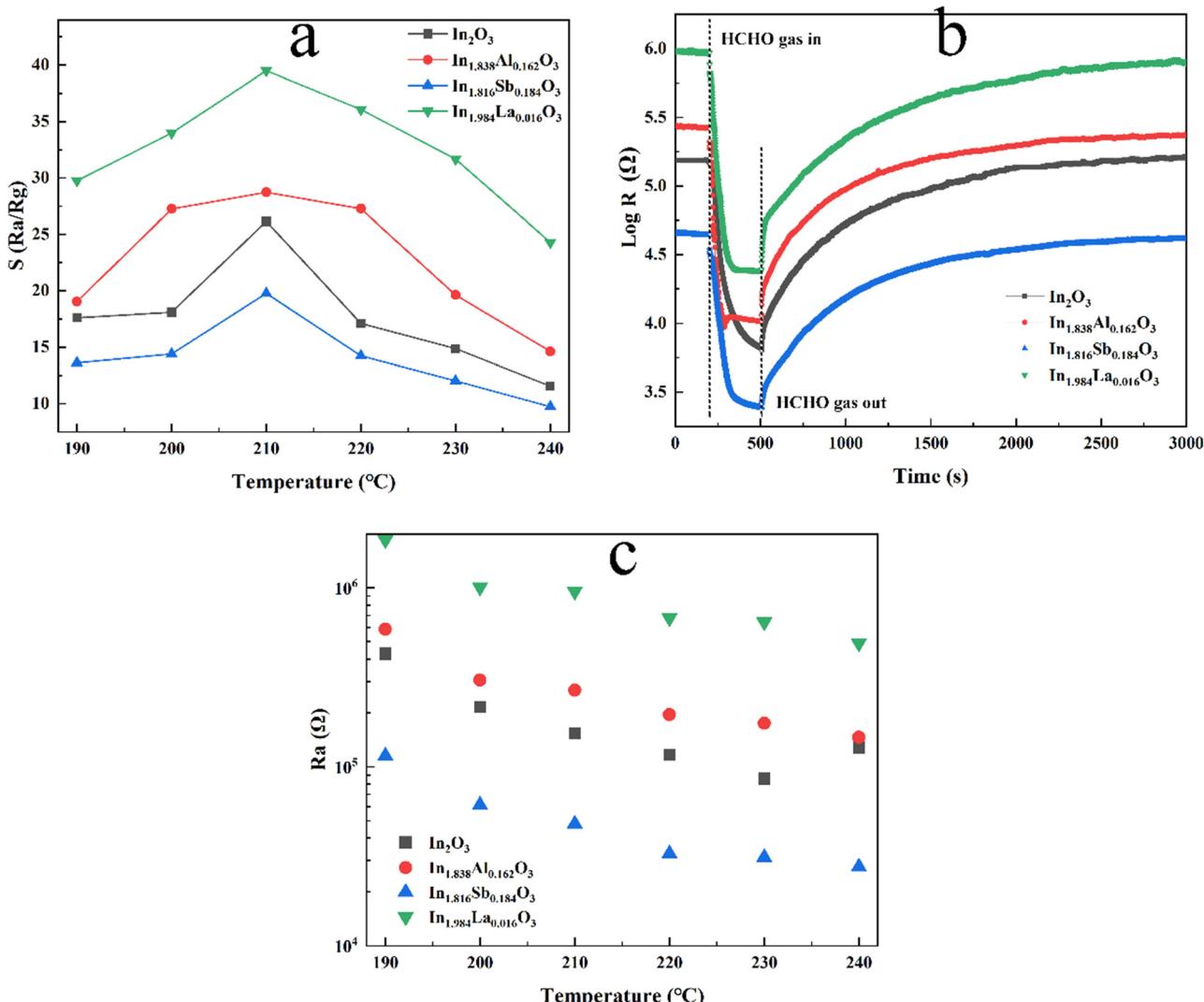
Fig. 7 (a) Response of In_2O_3, and Al-, Sb- and La-doped In_2O_3 NW sensors to 10 ppm HCHO gas at different operating temperatures; (b) response and recovery curves of all the sensors to 10 ppm HCHO gas at 210 °C; and (cs) R_{air} values for all sensors at the different operating temperatures.

sensors is 80 s, 33 s, 77 s and 50 s, respectively. The response time of the cation-doped In_2O_3 NWs sensors is shorter than for the In_2O_3 NW sensor. This should be attributed to the destruction of the periodic potential field for cation doping, which facilitates the diffusion of molecular oxygen.[40]

The influence of the HCHO gas concentration from 1 ppm to 15 ppm on the response of In_2O_3 and the cation-doped In_2O_3 NW sensors at 210 °C is also discussed in Fig. 8(a). It was seen that the response of all the sensors increases with the HCHO

gas concentration. HCHO gas first reacts with the adsorbed oxygen, and re-injects the extracted electrons back to the shell of In_2O_3 and the cation-doped In_2O_3 NWs. As the result, the resistance decreases greatly when in HCHO gas. The higher the HCHO gas concentration, the lower is the resistance value of all the sensors. Therefore, the response to HCHO gas increases greatly with the HCHO gas concentration for all sensors. Moreover, the relationship between the response (S) and the HCHO gas concentration (C) can be expressed in eqn (3) as:

$$S = a(C)^b + 1 \qquad (3)$$

where a and b are constants.[29] Based on the data in Fig. 8(a), a and b can be calculated using eqn (3). The above equation can therefore be rewritten as:

$$\log(S - 1) = b\log(C) + \log(a). \qquad (4)$$

In this way, the relationship between $\log(S - 1)$ and $\log(C)$ is plotted in Fig. 8(b) for In_2O_3 and the cation-doped In_2O_3 NW

Table 2 Resistance values of all sensors in air and 10 ppm HCHO gas at 210 °C

| Sample	R_{air} (Ω)	R_{gas} (Ω)
In_2O_3 NWs	153 644	6650
$In_{1.838}Al_{0.162}O_3$ NWs	267 635	10 389
$In_{1.816}Sb_{0.184}O_3$ NWs	47 943	2424
$In_{1.984}La_{0.016}O_3$ NWs	954 557	24 202
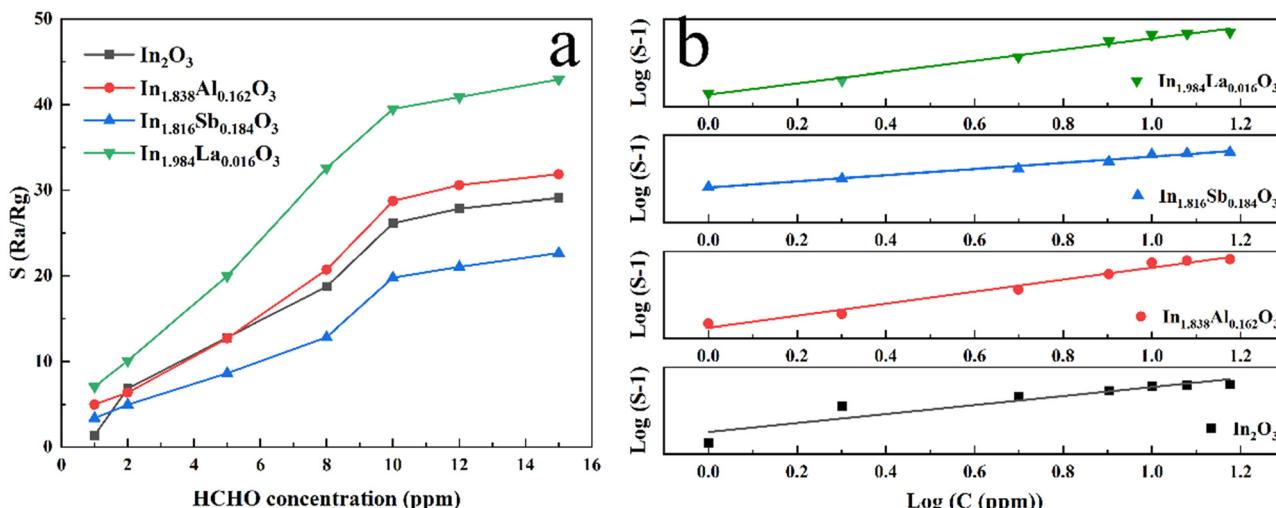
Fig. 8 Concentration-dependent response curves (a) and the predicted concentration-response curves (b) for In_2O_3 and the cation-doped In_2O_3 NW sensors to HCHO gas at 210 °C.

sensors, in which the response exhibits a good linear relationship with the HCHO gas concentration. Therefore, the HCHO gas concentration can be easily predicted according to the response value, indicating an excellent application in practice.

Furthermore, the selectivity of all the sensors towards 10 ppm ethanol, ammonia gas (ammonia water changed to ammonia gas after evaporation), water vapor, xylene, toluene, methanol and HCHO gases at 210 °C are given in Fig. 9(a). All sensors exhibit a much smaller response to water vapor than that of HCHO gas, indicating that the influence of humidity on the gas-sensing performance can be ignored. Clearly, the response to HCHO gas presents the highest value of all the gases, which indicates the excellent selectivity of the sensor to HCHO gas. In order to investigate the stability of In_2O_3 and the cation-doped In_2O_3 NW sensors, the response to 10 ppm HCHO gas was tested 5 times at 210 °C, as shown in Fig. 9(b).

The response of all the sensors hardly changes, indicating the long-term stability of In_2O_3 and the cation-doped In_2O_3 NWs. Compared with the work of other researchers, the response to HCHO gas using the different gas-sensing media is listed in Table 3, in which the $In_{1.984}La_{0.016}O_3$ NW sensor presents one of the highest responses to 10 ppm HCHO gas with an S value of about 40.

3.3 Gas-sensing mechanism of cation-doped In_2O_3 NW sensors

For In_2O_3 and the cation-doped In_2O_3 NWs in air, the higher surface area adsorbed more oxygen molecules on the surface. The adsorbed oxygen molecules extract electrons from the surface shell and become O^- at 210 °C to form an electron-depletion layer.[38] As a result, the shell resistance in air ($R_{shell(air)}$) increases dramatically owing to the high surface area
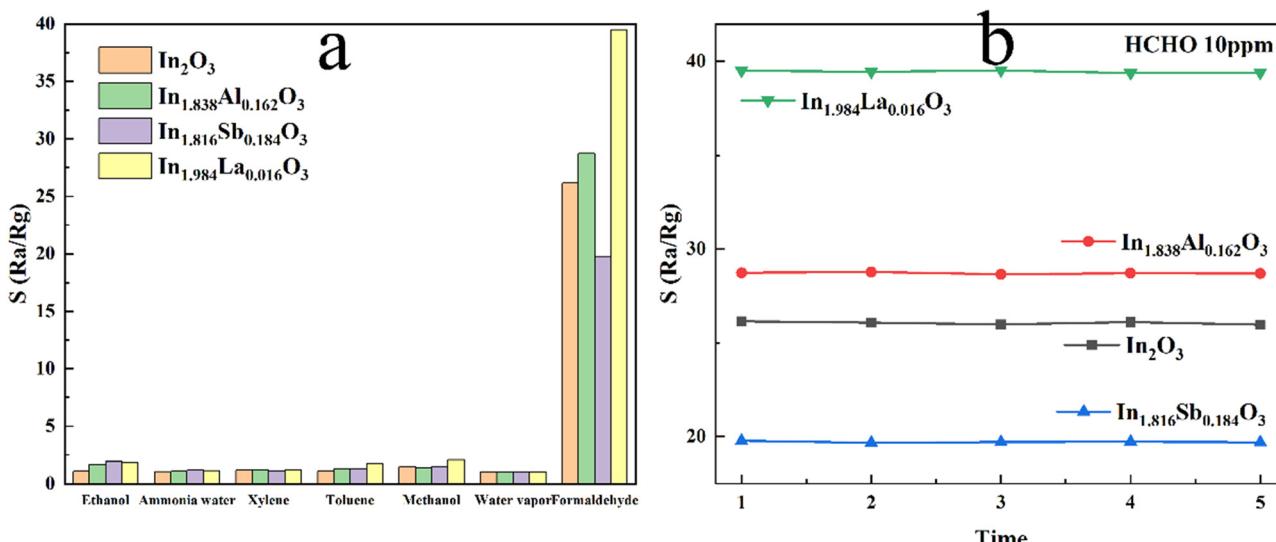

Fig. 9 Selectivity (a) and long-term stability (b) of In_2O_3 and the cation-doped In_2O_3 NW sensors.

Table 3 HCHO gas-sensing properties of the different sensing media

Sensing material	T_{sens} (°C)	HCHO concentration (ppm)	S	Ref.
α-Fe₂O₃ particles	270	500	23	30
ZnSnO₃ cubic	180	30	25	31
rGO/ZnSnO₃ microspheres	110	10	12	32
In₂O₃@rGO nanocubes	225	25	88	33
WO$_x$/In₂O₃ nanosheets	170	100	25	34
SnO₂ nanowires	270	10	2.45	35
Er-doped porous In₂O₃ nanotubes	260	20	12	36
2 at% Al-doped ZnO	320	50	6.8	37
In$_{1.984}$La$_{0.016}$O₃ NWs	210	10	39.51	This work

of the mesoporous structures. The more adsorptive O^- that are present, the thicker electron-depletion layer, as shown in Fig. 10. When HCHO gas is injected, the HCHO gas molecules prefer to react with O^- at the surface. The adsorptive O^- decreases with the increasing HCHO gas concentration and more and more electrons are re-injected back to the shell of In₂O₃ and the cation-doped In₂O₃ NWs. R_{gas} hardly changes without the adsorbed O^- at the extreme high concentration of HCHO gas. As a result, R_{gas} decreases and the response increases with the HCHO gas concentration.

The conduction pathway for n-type In₂O₃ NWs is equivalent to a series circuit of the core resistance (R_{core}) and shell resistance (R_{shell}).[29] In this way, the response can be rewritten as follows in eqn (5):

$$S = \frac{R_{air}}{R_{gas}} = \frac{R_{core} + R_{shell(air)}}{R_{core} + R_{shell(gas)}} = 1 + \frac{R_{shell(air)} - R_{shell(gas)}}{(R_{core} + R_{shell})_{gas}}$$
$$= 1 + \frac{\Delta R_{shell(air-gas)}}{R_{(gas)}} \quad (5)$$

If a higher response is wanted, $\Delta R_{shell(air-gas)}$ should be big enough and R_{gas} should be small as much as possible. The same-valent Al^{3+}, Sb^{3+} and La^{3+} ions that are substituted for In^{3+} in the In₂O₃ NWs hardly change the carrier concentration of the In$_{1.816}$Sb$_{0.184}$O₃, In$_{1.838}$Al$_{0.162}$O₃ and In$_{1.984}$La$_{0.016}$O₃ NWs compared with the undoped In₂O₃ NWs. Furthermore, the In₂O₃, In$_{1.838}$Al$_{0.162}$O₃, In$_{1.816}$Sb$_{0.184}$O₃ and In$_{1.984}$La$_{0.016}$O₃ NWs are synthesized using SBA-15 silica as a hard template under the same chemical conditions and calcination temperature, so the microstructures, morphology and defects of all the samples should be similar. Only in this way can the influence of the
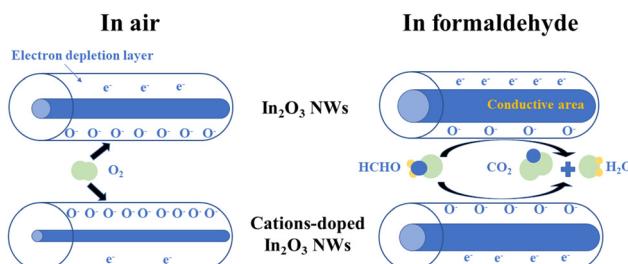
lattice distortion caused by cation doping on the gas-sensing performance of the In$_{1.816}$Sb$_{0.184}$O₃, In$_{1.838}$Al$_{0.162}$O₃ and In$_{1.984}$La$_{0.016}$O₃ NW sensors be truly revealed. As is known, cation-doping leads to lattice distortion of the In₂O₃ NWs for the different cation radii, resulting in a change in the oxygen vacancy concentration or chemical state of the adsorbed ions on the surface.[39] At the same time, cation doping causes destruction of the periodic potential field, making the In₂O₃ lattice more open, which facilitates the diffusion of molecular oxygen through the In₂O₃ lattice.[40]

The radii of Al^{3+} (0.0535 nm) and La^{3+} (0.1032 nm) present a larger difference with that of In^{3+} (0.080 nm), whereas Sb^{3+} (0.076 nm) possesses a similar radius to In^{3+}.[41] Doping with the large La^{3+} radius causes the largest lattice distortion for the In$_{1.984}$La$_{0.016}$O₃ NW lattice whereas doping with Al^{3+} and Sb^{3+}, which have a smaller radius than La^{3+}, bring about a smaller lattice distortion, as shown in schematic diagram in Fig. 11. Moreover, the cation-doped In₂O₃ NWs present the similar specific surface areas with a value of about 50 m² g⁻¹, which possesses the similar adsorbed oxygen owing to the mesoporous structures.[42] As shown in Fig. 10, the larger lattice distortion results in more oxygen vacancies, which leads to the more adsorbed oxygen on the surface of the cation-doped In₂O₃ NWs.[22] It was reported that rare-earth doping increases the surface alkalinity, which further improves the adsorbed oxygen of the In$_{1.984}$La$_{0.016}$O₃ NWs.[43] The more adsorbed oxygen leads to a larger change of $\Delta R_{shell(air-gas)}$ according to eqn (5) for the In$_{1.984}$La$_{0.016}$O₃ NWs sensor.

Moreover, cation-doping generates the lattice distortion of the In$_{1.816}$Sb$_{0.184}$O₃, In$_{1.838}$Al$_{0.162}$O₃ and In$_{1.984}$La$_{0.016}$O₃ NWs, which scatters the electron transport and increases the R_{gas} value. The cation-doping content increases from In$_{1.984}$La$_{0.016}$O₃ to In$_{1.838}$Al$_{0.162}$O₃ and In$_{1.816}$Sb$_{0.184}$O₃ NWs, leading to the highest R_{gas} for the In$_{1.816}$Sb$_{0.184}$O₃ NWs and the lowest R_{gas} for the In$_{1.984}$La$_{0.016}$O₃ NWs. According to eqn (5), the response of all the sensors to HCHO gas increases from 19.78 for In$_{1.816}$Sb$_{0.184}$O₃ to 26.16 for In₂O₃, 28.73 for In$_{1.838}$Al$_{0.162}$O₃ and 39.51 for In$_{1.984}$La$_{0.016}$O₃. La-doping not only improves the adsorbed oxygen on the surface of the In₂O₃ NW sensor but also increases R_{gas}. Compared with the In₂O₃, In$_{1.816}$Sb$_{0.184}$O₃ and In$_{1.838}$Al$_{0.162}$O₃ NW


Fig. 10 Theoretical schematic of the electron-depletion layer for In₂O₃ and the cation-doped In₂O₃ NWs in air and formaldehyde.
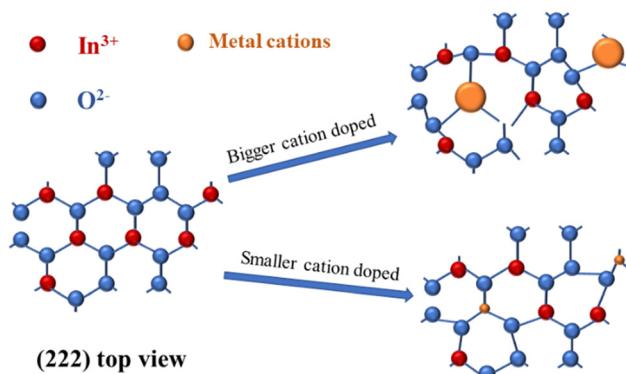

Fig. 11 Schematic diagram of lattice distortion for In₂O₃ and the cation-doped In₂O₃ NWs.

sensors, the $In_{1.984}La_{0.016}O_3$ NW sensor presents the highest response owing to the larger lattice distortion and the lowest doping content.

4. Conclusions

Mesoporous In_2O_3 and cation-doped In_2O_3 NWs have been synthesized using a nanocasting method. Different metals (Al, Sb and La) have been introduced to study the influence on the sensing performance. The characterization results show that both cation-doped In_2O_3 and undoped In_2O_3 NWs have a long-range-order mesoporous structure with a high specific surface area. All sensors present the best gas-sensing performance at the optimal working temperature of 210 °C, and the response of the La-doped In_2O_3 NWs reaches the maximum value of 39.51 for 10 ppm HCHO gas. The cation doping not only brings about lattice distortion to improve the adsorbed oxygen on the surface but also increases the ground-state resistance of the In_2O_3 NWs. Rare-earth doping increases the surface alkalinity, improving the sensor response towards HCHO. La-doping increases both the adsorbed oxygen and the lattice distortion of La-doped In_2O_3 NWs, and is responsible for the highly enhanced HCHO gas-sensing performance of the $In_{1.984}La_{0.016}O_3$ NWs sensor.

Conflicts of interest

The authors declare that they have no conflict of interest.

Acknowledgements

References

1 N. Letellier, L. A. Gutierrez, C. Pilorget, F. Artaud, A. Descatha, A. Ozguler, M. Goldberg, M. Zins, A. Elbaz and C. Berr, Association Between Occupational Exposure to Formaldehyde and Cognitive Impairment, *Neurology*, 2022, **98**, E633–E640.

2 T. Salthammer, S. Mentese and R. Marutzky, Formaldehyde in the indoor enviorment, *Chem. Rev.*, 2010, **110**, 2536–2572.

3 T. Y. Zhong, H. X. Li, T. M. Zhao, H. Y. Guan, L. L. Xing and X. Y. Xue, Self-powered/self-cleaned atmosphere monitoring system from combining hydrovoltaic, gas sensing and photocatalytic effects of TiO_2 nanoparticles, *J. Mater. Sci. Technol.*, 2021, **76**, 33–40.

4 T. A. Vincent, Y. X. Xing, M. Cole and J. W. Gardner, Investigation of the response of high-bandwidth MOX sensors to gas plumes for application on a mobile robot in hazardous environments, *Sens. Actuators, B*, 2019, **279**, 351–360.

5 Y. H. Kim, P. Kumar, E. E. Kwon and K. H. Kim, Metal-organic frameworks as superior media for thermal desorption-gas chromatography application: A critical assessment of MOF-5 for the quantitation of airborne formaldehyde, *Microchem. J.*, 2017, **132**, 219–226.

6 P. Wahed, M. A. Razzaq, S. Dharmapuri and M. Corrales, Determination of formaldehyde in food and feed by an in-house validated HPLC method, *Food Chem.*, 2016, **202**, 476–483.

7 X. C. Qin, R. Wang, F. Tsow, E. Forzani, X. J. Xian and N. J. Tao, A colorimetric chemical sensing platform for real-time monitoring of indoor formaldehyde, *IEEE Sens. J.*, 2015, **15**, 1545–1551.

8 B. M. Woolston, T. Roth, I. Kohale, D. R. Liu and G. Stephanopoulos, Development of a formaldehyde bio-sensor with application to synthetic methylotrophy, *Biotechnol. Bioeng.*, 2018, **115**, 206–215.

9 J. N. Mao, B. Hong, H. D. Chen, M. H. Gao, J. C. Xu, Y. B. Han, Y. T. Yang, H. X. Jin, D. F. Jin, X. L. Peng, J. Li, H. L. Ge and X. Q. Wang, Highly improved ethanol gas response of n-type α-Fe_2O_3 bunched nanowires sensor with high-valence donor-doping, *J. Alloys Compd.*, 2020, **827**, 154248.

10 J. Q. Wei, X. Q. Li, Y. B. Han, J. C. Xu, H. X. Jin, D. F. Jin, X. L. Peng, B. Hong, J. Li, Y. T. Yang, H. L. Ge and X. Q. Wang, Highly improved ethanol gas-sensing performance of mesoporous nickel oxides nanowires with the stannum donor doping, *Nanotechnology*, 2018, **29**, 245501.

11 X. Q. Li, J. Q. Wei, J. C. Xu, H. X. Jin, D. F. Jin, X. L. Peng, B. Hong, J. Li, Y. T. Yang, H. L. Ge and X. Q. Wang, Highly improved sensibility and selectivity ethanol sensor of meso-porous Fe-doped NiO nanowires, *J. Nanopart. Res.*, 2017, **19**, 396.

12 D. P. Li, B. B. Zhang, J. C. Xu, Y. B. Han, H. X. Jin, D. F. Jin, X. L. Peng, H. L. Ge and X. Q. Wang, Wide bandgap mesoporous hematite nanowire bundles as a sensitive rapid response ethanol sensor, *Nanotechnology*, 2016, **27**, 185702.

13 X. Q. Li, D. P. Li, J. C. Xu, Y. B. Han, H. X. Jin, B. Hong, H. L. Ge and X. Q. Wang, Calcination-temperature-dependent gas-sensing properties of mesoporous α-Fe_2O_3 nanowires as ethanol sensors, *Solid State Sci.*, 2017, **69**, 38–43.

14 D. Im, D. Kim, D. Jeong, W. I. Park, M. Chun, J. S. Park, H. Kim and H. Jung, Improved formaldehyde gas sensing properties of well-controlled Au nanoparticle-decorated In_2O_3 nanofibers integrated on low power MEMS platform, *J. Mater. Sci. Technol.*, 2021, **38**, 56–63.

15 T. T. Zhou and T. Zhang, Recent progress of nanostructured sensing materials from 0D to 3D: overview of structure-property-application relationship for gas sensors, *Small, Methods*, 2021, **5**, 2100515.

16 L. Wang, S. Y. Song, B. Hong, J. C. Xu, Y. B. Han, H. X. Jin, D. F. Jin, J. Li, Y. T. Yang, X. L. Peng, H. L. Ge and X. Q. Wang, Highly improved toluene gas-sensing performance of mesoporous Co_3O_4 nanowires and physical mechanism, *Mater. Res. Bull.*, 2021, **140**, 111329.

17 M. Hassan, Z. H. Wang, W. R. Huang, M. Q. Li, J. W. Liu and J. F. Chen, Ultrathin tungsten oxide nanowires/reduced graphene oxide composites for toluene sensing, *Sensors*, 2017, **17**, 2245.

18 X. Q. Li, D. P. Li, J. C. Xu, H. X. Jin, D. F. Jin, X. L. Peng, B. Hong, J. Li, Y. T. Yang, H. L. Ge and X. Q. Wang, Mesoporous-structure enhanced gas-sensing properties of nickel oxides nanowires, *Mater. Res. Bull.*, 2017, **89**, 280–285.

19 H. D. Chen, K. L. Jin, J. C. Xu, Y. B. Han, H. X. Jin, D. F. Jin, X. L. Peng, B. Hong, J. Li, Y. T. Yang, J. Gong, H. L. Ge and X. Q. Wang, High-valence cation-doped mesoporous nickel oxides nanowires: nanocasting synthesis, microstructures and improved gas-sensing performance, *Sens. Actuators, B*, 2019, **296**, 126622.

20 H. D. Chen, K. L. Jin, P. F. Wang, J. C. Xu, Y. B. Han, H. X. Jin, D. F. Jin, X. L. Peng, B. Hong, J. Li, Y. T. Yang, J. Gong, H. L. Ge and X. Q. Wang, Highly enhanced gas-sensing properties of indium-doped mesoporous hematite nanowires, *J. Phys. Chem. Solids*, 2018, **120**, 271–278.

21 T. P. Mokoena, H. C. Swart, K. T. Hillie and D. E. Motaung, Engineering of rare-earth Eu^{3+} ions doping on n-type NiO for selective detection of toluene gas sensing and luminescence properties, *Sens. Actuators, B*, 2021, **347**, 130530.

22 W. H. Zhang, S. J. Ding, Q. S. Zhang, H. Yi, Z. X. Liu, M. L. Shi, R. F. Guan and L. Yue, Rare earth element-doped porous In_2O_3 nanosheets for enhanced gas-sensing performance, *Rare Met.*, 2021, **40**, 1662–1668.

23 X. H. Jin, Y. W. Li, B. Zhang, X. T. Xu, G. Sun and Y. Wang, Temperature-dependent dual selectivity of hierarchical porous In_2O_3 nanospheres for sensing ethanol and TEA, *Sens. Actuators, B*, 2021, **330**, 129271.

24 X. J. Liu, X. Y. Tian, X. M. Jiang, L. Jiang, P. Y. Hou, S. W. Zhang, X. Sun, H. C. Yang, R. Y. Cao and X. J. Xu, Facile preparation of hierarchical Sb-doped In_2O_3 microstructures for acetone detection, *Sens. Actuators, B*, 2018, **270**, 304–311.

25 Q. H. Liang, X. X. Zou, H. Chen, M. H. Fan and G. D. Li, High-performance formaldehyde sensing realized by alkaline-earth metals doped In_2O_3 nanotubes with optimized surface properties, *Sens. Actuators, B*, 2020, **304**, 127241.

26 Z. H. Wang, C. L. Hou, Q. M. De, F. B. Gu and D. M. Han, One-Step synthesis of Co-doped In_2O_3 nanorods for high response of formaldehyde sensor at low temperature, *ACS Sens.*, 2018, **3**, 468–475.

27 X. Y. Wang, J. J. Ma, Q. Ren, M. M. Wang, Z. Yang and J. H. Xin, Effects of Fe^{3+}-doping and nano-TiO_2/WO_3 decoration on the ultraviolet absorption and gas-sensing properties of $ZnSnO_3$ solid particles, *Sens. Actuators, B*, 2021, **344**, 130223.

28 P. F. Cheng, Y. L. Wang, C. Wang, J. Ma, L. P. Xu, C. Lv and Y. F. Sun, Investigation of doping effects of different noble metals for ethanol gas sensors based on mesoporous In_2O_3, *Nanotechnology*, 2021, **32**, 305503.

29 L. Wang, B. Hong, H. D. Chen, J. C. Xu, Y. B. Han, H. X. Jin, D. F. Jin, X. L. Peng, H. L. Ge and X. Q. Wang, The highly improved gas-sensing performance of α-Fe_2O_3-decorated NiO nanowires and the interfacial effect of p-n heterojunctions, *J. Mater. Chem. C*, 2020, **8**, 3855–3864.

30 W. X. Jin, S. Y. Ma, Z. Z. Tie, X. H. Jiang, W. Q. Li, J. Luo, X. L. Xu and T. T. Wang, Hydrothermal synthesis of mono-disperse porous cube, cake and spheroid-like α-Fe_2O_3 particles and their high gas-sensing properties, *Sens. Actuators, B*, 2015, **220**, 243–254.

31 W. W. Guo, B. Y. Zhao, L. L. Huang and Y. Z. He, One-step synthesis of $ZnWO_4/ZnSnO_3$ composite the enhanced gas sensing performance to formaldehyde, *Mater. Lett.*, 2020, **277**, 128327.

32 J. H. Sun, S. L. Bai, Y. Tian, Y. H. Zhao, N. Han, R. X. Luo, D. Q. Li and A. F. Chen, Hybridization of $ZnSnO_3$ and rGO for improvement of formaldehyde sensing properties, *Sens. Actuators, B*, 2018, **257**, 29–36.

33 R. K. Mishra, G. Murali, T. H. Kim, J. H. Kim, Y. J. Lim, B. S. Kim, P. P. Sahay and S. H. Lee, Nanocube In_2O_3@rGO heterostructure based gas sensor for acetone and formaldehyde detection, *RSC Adv.*, 2017, **7**, 38714–38724.

34 Y. Y. Cao, Y. He, X. X. Zou and G. D. Li, Tungsten oxide clusters decorated ultrathin In_2O_3 nanosheets for selective detecting formaldehyde, *Sens. Actuators, B*, 2017, **252**, 232–238.

35 I. Castro-Hurtado, J. Gonzalez-Chavarri, S. Morandi, J. Sama, A. Romano-Rodriguez, E. Castano and G. G. Mandayo, Formaldehyde sensing mechanism of SnO_2 nanowires grown on-chip by sputtering techniques, *RSC Adv.*, 2016, **6**, 18558–18566.

36 X. S. Wang, J. B. Zhang, L. Y. Wang, S. C. Li, L. Liu, C. Su and L. L. Liu, High response gas sensors for formaldehyde based on Er-doped In_2O_3 nanotubes, *J. Mater. Sci. Technol.*, 2015, **31**, 1175–1180.

37 K. Khojier, Preparation and investigation of Al-doped ZnO thin films as a formaldehyde sensor with extremely low detection limit and considering the effect of RH, *Mater. Sci. Semicond. Process.*, 2020, **121**, 105283.

38 R. Prajesh, V. Goyal, M. Nahid, V. Saini, A. K. Singh, A. K. Sharma, J. Bhargava and A. Agarwal, Nickel oxide (NiO) thin film optimization by reactive sputtering for highly sensitive formaldehyde sensing, *Sens. Actuators, B*, 2020, **318**, 128166.

39 S. K. Zhao, Y. B. Shen, A. Li, Y. S. Chen, S. L. Gao, W. G. Liu and D. Z. Wei, Effects of rare earth elements doping on gas sensing properties of ZnO nanowires, *Ceram. Int.*, 2021, **47**, 24218–24226.

40 Z. H. Wang, Z. W. Tian, D. M. Han and F. B. Gu, Highly sensitive and selective ethanol sensor fabricated with In-doped 3DOM ZnO, *ACS Appl. Mater. Interfaces*, 2016, **8**, 5466–5474.

41 R. D. Shannon, Revised effective ionic radii and systematic studied of interatomic distances in halides and chalcogenides, *Acta Crystallogr.*, 1976, **32**, 751–767.

42 J. Zhao, W. N. Wang, Y. P. Liu, J. M. Ma, X. W. Li, Y. Du and G. Y. Lu, Ordered mesoporous Pd/SnO_2 synthesized by a nanocasting route for hydrogen sensing performance, *Sens. Actuators, B*, 2011, **160**, 604–608.

43 A. Hastir, N. Kohli and R. C. Singh, Comparative study on gas sensing properties of rare earth (Tb, Dy and Er) doped ZnO sensor, *J. Phys. Chem. Solids*, 2017, **105**, 23–34.